UMERC+OREC
2025 Conference

12-14 August | Corvallis, OR USA

Experimentally Validated Numerical Modeling and Control for Optimizing PTO Efficiency in Wave Energy Converters

Shangyan Zou[a] [1], Tim Donnelly[b], Wayne Weaver[a], Giorgio Bacelli[c], David Wilson[b]

[a]*Department of Mechanical and Aerospace Engineering, Michigan Technological University, Houghton 49931, United States*
[b]*Electrical Sciences, Sandia National Laboratories, Albuquerque, NM 87158, Unites States*
[b]*Water Power Technologies, Sandia National Laboratories, Albuquerque, NM 87158, Unites States*

Abstract

This paper presents the calibration of a high-fidelity Power Take-Off (PTO) model for Wave Energy Converters (WECs) using experimental data from recent wave tank testing of the WaveBot device at the U.S. Navy's MASK Basin. The model integrates detailed representations of PTO control, motor dynamics, and inverter behavior, including switching-level simulation of power electronics. By tuning the model parameters, this study demonstrates good agreement between simulated and measured system responses and losses. The experimentally calibrated model serves as a foundation for optimal control design of WECs to maximize PTO efficiency. More specifically, a novel control that enables a time-varying DC bus voltage is proposed, and the simulation results show a 62% reduction in inverter losses, which improves the PTO efficiency by 48.5% compared to an unoptimized PTO architecture.

Keywords: Wave Energy Converter; Power Take-Off; Wave Tank Testing; Model Calibration; Field-Oriented Control

[1] ∗ Corresponding author
E-mail address: shangyan@mtu.edu

1 Introduction

Ocean wave energy resources are abundant, consistent, and have a high power density compared to other renewable energy resources such as solar and wind [1]. In addition to supplying power to the grid, wave power also has its unique strength in supporting the growth of the blue economy, given that it is at-sea and available all day. Significant research efforts have been made in developing wave energy conversion technologies, including hydrodynamic modeling [2, 3, 4], PTO control [5, 6, 7], resource assessment [8, 9, 10], mooring design [11], etc. However, wave energy conversion technology is still in its infancy, and many challenges need to be addressed to facilitate its economic viability.

One long-standing challenge of state-of-the-art WEC technologies is the inefficient conversion of mechanical power into useful electricity. A large volume of literature focuses on developing advanced controls that maximize the mechanical power production of the WEC; however, it often overlooks the losses in the PTO unit. This typically leads to significantly degraded electrical power generation or even negative power, which poses significant concerns for practical applications [12]. Only limited studies in the literature are dedicated to understanding the performance and developing controls for the power electronics in the PTO unit [13, 14], which is the major source of power losses.

To address this gap, the authors have recently developed a high-fidelity wave-to-wire model that holistically considers hydrodynamics, PTO control, Permanent Magnet Synchronous Motor (PMSM) dynamics, and inverter dynamics [15]. The dynamic behavior of the power electronics is directly simulated (to the level of transistors), with losses comprehensively considered, including motor copper losses, inverter conduction losses, and switching losses, aiming to accurately capture the losses in the PTO unit. This preliminary study found that the DC bus voltage and switching frequency have a significant impact on PTO losses. It is also found the PTO energy conversion efficiency can be improved by up to 61.78% under optimal DC voltage and switching frequency compared to the unoptimized case. This indicates significant opportunities exist in customizing the designs for PTO unit for specific WECs rather than directly employing Commercial Off-the-Shelf (COTS) components which are typically overdesigned for WEC applications.

Despite the opportunities presented, the developed high-fidelity model is not calibrated with experimental data (although model parameters are set to match the real hardware) in terms of detailed system responses and losses. Therefore, building upon this prior effort, we will further improve the model fidelity by calibrating it using detailed experimental testing data in this study. As far as the experimental data is concerned, the research team at Sandia National Laboratories (SNL) conducted wave tank tests of the WaveBot device at the U.S. Navy's Maneuvering and Sea Keeping (MASK) Basin and published the open-source testing data [16]. It is noted that this test focuses on investigating the PTO performance, and rich measurements were collected, including three-phase current/voltage, DC current/voltage, motor torque, velocity, and power measured on the mechanical side, AC side, and DC side under varied wave conditions. This data is leveraged in this study to adjust the high-fidelity PTO model to ensure the model accurately predicts both dynamic responses and losses. The calibrated model is then simulated across different wave conditions and parameter setups to present the impact of key parameters on system efficiency. In addition to the modeling effort, a new control that allows a time-varying DC bus voltage is also derived in this study. This time-varying DC bus voltage represents the minimum voltage required to supply the desired instantaneous PTO torque, which significantly reduces losses in the PTO drivetrain.

This paper is organized as follows: the modeling and control are introduced in Section. II, and the results are discussed in Section. III. Finally, the conclusion is drawn in Section. IV.

2 Methodology

The complete configuration of the drivetrain of WaveBot is presented in Fig. 1. Specifically, the heave motion of the WaveBot is converted into rotational motion through a rack-and-pinion mechanism. This rotational motion then drives the rotor of a PMSM, generating three-phase electrical power. The generated AC power is subsequently converted to DC via an AC/DC inverter, which controls the torque output of the electric machine by regulating the AC voltage.

It is worth noting that this study focuses on the model calibration only for the PTO unit. More specifically, the modeling of the mechanical side, which includes the hydrodynamics as well as the model for the magnetic spring (which is incorporated to physically provide a negative spring effect) [16], is not considered. Instead, the direct measurements of the mechanical side of the complete system (e.g., the buoy velocity, PTO force, and motor angle) will be applied as inputs to the PTO model to simulate the PTO performance. This is because there exist uncertainties and nonlinearities in the dynamics on the mechanical side, and modeling this part itself is a nontrivial task that is currently beyond the scope of this study.

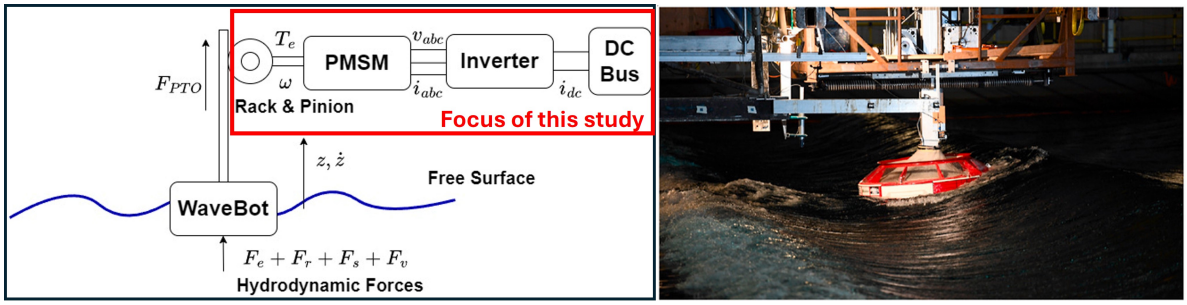

Figure 1: Overall wave-to-wire configuration. It is noted that this paper focuses on the PTO unit.

Furthermore, this section will first introduce the high-fidelity model of the PTO unit. Next, the detailed derivation of the new control that enables a time-varying DC bus voltage will be presented.

2.1 PTO model

The high-fidelity PTO model is developed in Simscape/Simulink, and is mainly composed of the PMSM, motor drive, and the DC bus. Given that this model does not simulate the hydrodynamic behavior of the WEC, it receives the measured velocity (of the WEC) and the commanded PTO force as inputs and simulates the actual PTO force output, which aligns with the working mechanism of the PTO unit in practice.

2.1.1 Permanent Magnet Synchronous Motor

Physically, the PMSM is driven by the linear motion of WaveBot via a rack and pinion system (which converts the linear motion to rotation), as presented in Fig. 1. The PMSM is controlled by the motor drive to produce the desired three-phase current, such that it supplies a desired PTO force acting on the WEC. It is typically challenging to directly work with the motor model in the ABC domain; therefore, the rotating reference frame method is applied:

$$\begin{bmatrix} d \\ q \\ 0 \end{bmatrix} = \frac{2}{3} \begin{bmatrix} \cos(\theta_e) & \cos(\theta_e - \frac{2\pi}{3}) & \cos(\theta_e + \frac{2\pi}{3}) \\ -\sin(\theta_e) & -\sin(\theta_e - \frac{2\pi}{3}) & -\sin(\theta_e + \frac{2\pi}{3}) \\ \frac{1}{2} & \frac{1}{2} & \frac{1}{2} \end{bmatrix} \begin{bmatrix} a \\ b \\ c \end{bmatrix} \tag{1}$$

Here, the transformation between the ABC and the DQ frames is the Park transformation. θ_e denotes the electrical rotor angle, which is computed as the product of the number of pole pairs (n_p) and the mechanical rotor angle (θ_m), i.e., $\theta_e = n_p \times \theta_m$. After conducting the transformation, the resulting motor dynamics is:

$$\begin{aligned} v_d &= R_s i_d + L_d \dot{i}_d - n_p \omega i_q L_q \\ v_q &= R_s i_q + L_q \dot{i}_q + n_p \omega (i_d L_d + \psi_m) \end{aligned} \tag{2}$$

In this equation, R_s represents the equivalent resistance of the stator windings, while L_d and L_q denote the stator inductance along the d-axis and q-axis, respectively. Additionally, ψ_m refers to the flux linkage of the permanent magnet. Furthermore, the resulting motor torque is calculated as:

$$T_e = \frac{3}{2} n_p (i_q (i_d L_d + \psi_m) - i_d i_q L_q) \tag{3}$$

The actual motor used in the experimental campaign is Applied Motion MF0310100-C0X, and the specifications of the motor provided by the manufacturer can be found in [17]. These parameters will be further tuned subject to the experimental data.

2.1.2 Motor Drive

The motor drive is composed by six Insulated Gate Bipolar Transistor (IGBT) switches with a standard three-phase two-level architecuture. In the proposed high-fidelity model, the behaviors of these switches are explicitly modelled

(such that the model can accurately predict the switching losses and conduction losses). The model of a single IGBT is:

$$i_{CE} = \begin{cases} \dfrac{v_{CE} - v_f(1 - R_{on}G_{off})}{R_{on}}, & \text{if } v_{CE} > v_f \ \& \ G > v_{th} \\ v_{CE}G_{off}, & \text{otherwise} \end{cases} \tag{4}$$

In this equation, i_{CE} and v_{CE} refer to the collector-emitter current and voltage, respectively. G denotes the gate voltage, v_f is the forward voltage, and v_{th} represents the threshold voltage. Moreover, R_{on} and G_{off} correspond to the on-state resistance and off-state conductance, respectively. Moreover, the diode is implemented in parallel with the IGBT, which is also modeled using the piecewise linear model. It is noted that a fixed junction capacitance is added to the diode. Both the conduction losses and switching losses in the drive are considered. In this case, the conduction losses are directly reflected in the system responses. To avoid excessive computational cost, the heat transfer mechanism of the switches is not modeled. Instead, the switching losses are calculated according to the on and off events of the switches, and for each event, the losses are modeled as:

$$E_{on} = E_{on,0}\frac{v_{CE}}{v_{CE,nom}}\frac{i_{CE}}{i_{CE,nom}} \tag{5}$$

$$E_{off} = E_{off,0}\frac{v_{CE}}{v_{CE,nom}}\frac{i_{CE}}{i_{CE,nom}} \tag{6}$$

where $E_{on,0}$ and $E_{off,0}$ are the on and off losses measured at $v_{CE,nom}$ and $i_{CE,nom}$, respectively. The calibrated parameters of the IGBT and Diode will be summarized in the results section.

2.1.3 Field Oriented Control

A standard Field Oriented Control (FOC) is applied in the PTO unit to produce the desired PTO force. It is noted that this control differs from the new DC bus voltage control that will be presented in the next section, which has a control objective of minimizing the power losses in the drivetrain under certain load and speed conditions. The FOC control defines the desired DQ frame current according to the PTO force command as:

$$\begin{aligned} i_{d,ref} &= 0 \\ i_{q,ref} &= T_{e,ref}\frac{2}{3n_p\psi_m} \end{aligned} \tag{7}$$

where the reference motor torque can be computed from the command PTO force as: $T_{e,ref} = F_{PTO,ref}r_m$. The FOC control then receives the feedback signals on the three-phase current and computes the control by applying a proportional-integral (PI) control law:

$$v_{d,ref} = K_{p,d}(i_d - i_{d,ref}) + K_{i,d}\int (i_d - i_{d,ref})dt \tag{8}$$

$$v_{q,ref} = K_{p,q}(i_q - i_{q,ref}) + K_{i,q}\int (i_q - i_{q,ref})dt \tag{9}$$

Here, $K_{p,d}$, $K_{p,q}$, $K_{i,d}$, and $K_{i,q}$ are the proportional and integral gains of the PI control respectively. The resulting current control $v_{d,ref}$ and $v_{q,ref}$ will be transferred to the reference voltage in three-phase and supplied using a space vector Pulse Width Modulation (SVPWM) method (which controls the on and off of the switches).

2.1.4 DC bus voltage control

A novel control that is proposed in this study is the DC bus voltage control (DCVC). In a standard electrical drivetrain setup, the DC bus voltage is typically a constant value. It was found in our prior study [**<empty citation>**] that the DC bus voltage and the switching frequency have a significant impact on the PTO efficiency. More specifically, minimizing the DC bus voltage and switching frequency contributes to reducing the losses; however, this minimization is not unlimited. For instance, an extremely low switching frequency will significantly impact the tracking of the desired PTO force (e.g., dramatic rippling of the current/force) and also increase the losses. As far as the DC bus voltage is concerned, it cannot be too low, as it would otherwise fail to supply the voltage required by the PTO force.

Finding this lower limit is a challenging problem, especially for the DC bus voltage, given that it is dependent on the operational conditions (e.g., current and speed), which therefore are inherently time-varying. Accordingly, in this paper, we focus on deriving the lower limit of the DC bus voltage. Meanwhile, the minimum switching frequency is selected as the smallest constant value among those experimentally tested.
The derivation starts from the assumption that the DC bus voltage shall be sufficient to supply the desired three-phase voltage. The phase voltage can be computed as [18]:

$$\begin{aligned}
&\textbf{If } I_a > 0\textbf{, T+ conducting} : V_a = \frac{V_{dc}}{2} - I_a R_{on} \\
&\textbf{If } I_a > 0\textbf{, D- conducting} : V_a = -\frac{V_{dc}}{2} - I_a R_{on,d} \\
&\textbf{If } I_a < 0\textbf{, T- conducting} : V_a = -\frac{V_{dc}}{2} - I_a R_{on} \\
&\textbf{If } I_a < 0\textbf{, D+ conducting} : V_a = \frac{V_{dc}}{2} - I_a R_{on,d}
\end{aligned} \tag{10}$$

where in this equation, V_a and I_a represent the A phase voltage and current respectively. In addition, $T+$ and $D+$ denote the upper bridge IGBT and diode. Rearranging this equation, in order to supply the desired phase voltage, the DC bus voltage must satisfy:

$$\frac{V_{dc}}{2} \geq |V_a| + |I_a| R_{on} \tag{11}$$

Next, we need to derive the maximum magnitude of the phase voltage and current, and relate them to the operational conditions. In Eq. 2, we know that if the FOC control works properly, then at steady state:

$$\begin{aligned}
V_d &= n_p \omega i_q L_q \\
V_q &= R_s i_q + n_p \omega \psi_m
\end{aligned} \tag{12}$$

It is noted that, in addition to the differentiation terms, the i_d-related terms are also eliminated, given that the FOC control regulates the D-axis current to zero. Apply inverse Park Transformation, the voltage in the ABC frame can be expressed as (given that the system is balanced):

$$\begin{aligned}
V_a &= V_d \cos(\theta) - V_q \sin(\theta) \\
V_b &= V_d \cos(\theta - \frac{2\pi}{3}) - V_q \sin(\theta - \frac{2\pi}{3}) \\
V_c &= V_d \cos(\theta + \frac{2\pi}{3}) + V_q \sin(\theta + \frac{2\pi}{3})
\end{aligned} \tag{13}$$

It is clearly visible from this set of equations that the phase voltage has the same magnitude but a different phase shift, and:

$$|V_a| \leq \sqrt{V_d^2 + V_q^2} \tag{14}$$

Now we have obtained the upper bound of one term in the inequality presented in Eq. 11. With regard to $|I_a|$, this upper bound can be similarly derived by using the inverse Park Transformation:

$$|I_a| \leq \sqrt{I_d^2 + I_q^2} = |I_q| \tag{15}$$

Substitute Eq. 14 and 15 into Eq. 11, we can now derive the minimum DC bus voltage needed to supply the desired PTO force as:

$$V_{dc,min} = 2(\sqrt{V_d^2 + V_q^2} + |I_q| R_{on}) \tag{16}$$

where V_d and V_q in the equation will be computed using Eq. 12. Essentially, the minimum DC bus voltage is determined by the operational conditions: $V_{dc,min} = f(I_q, \omega)$.

3 Results

The results are presented in this section, which include the model calibration, system performance under varied operational conditions, and the performance of the new control. The simulations are performed in MATLAB/Simscape using a fixed-step solver with a time step of 2.5×10^{-7}s. The simulations are performed on a computer with an Intel Core i7–12700 2.10 GHz processor and 32 GB of RAM. The cost of a 20 s numerical simulation is around 3.6 hrs.

3.1 Model Calibration: Motor

The model calibration can be mainly divided into two parts: motor and inverter model calibration. The motor model is calibrated by matching certain system responses such as three-phase current and voltage, and the motor torque. Initially, the motor specifications provided by the manufacturer are directly applied in the numerical simulations, and the predicted system behavior is compared with the experimental data. The first mismatch found is the motor torque calculation. Under the FOC control, the motor torque shall be expressed as (based on Eq. 3):

$$T_e = \frac{3}{2} n_p \psi_m i_q = \frac{3}{2} K_t i_q \tag{17}$$

Both motor torque and the Q-axis current are measured experimentally, so it is relatively straightforward to identify the correct torque constant as: $K_t = 4.85$N/A instead of 7.186N/A (as provided by the manufacturer).
Next, Fig. 2 presents the comparison between the simulated and experimentally measured phase voltage and current (expressed in the Q frame). The corresponding wave condition has a height of 0.127m and a period of 3.3s. Moreover, the magnitude of the desired Q axis current is around 22.65A, and the resulting magnitude of the buoy velocity is around 0.472m/s. It is noted that the comparison between the phase voltage and current in the D frame is not presented since: (1) the D frame current is regulated to be zero under the FOC control; (2) the D frame voltage does not contribute to the active AC power calculation (only contributes to the reactive power). Therefore, the model tuning focuses on the alignment of Q axis voltage and current. However, we do observe a slight mismatch in the simulated and experimentally measured D axis voltage, which is likely due to the motor's nonlinear behavior. Given that this voltage does not impact the power calculation, the study of this nonlinear effect is out of the scope of the current study. It is clearly visible in the figure that the model provides a good prediction of the Q axis current. However, the predicted Q axis voltage exhibits a clear phase shift compared to the experimental data. This phase shift has a significant impact on the AC power calculation (as shown in Fig. 2(c)), where the numerically simulated AC power is 116.35W in contrast to 178.43W in the experimental data (34.8% error).

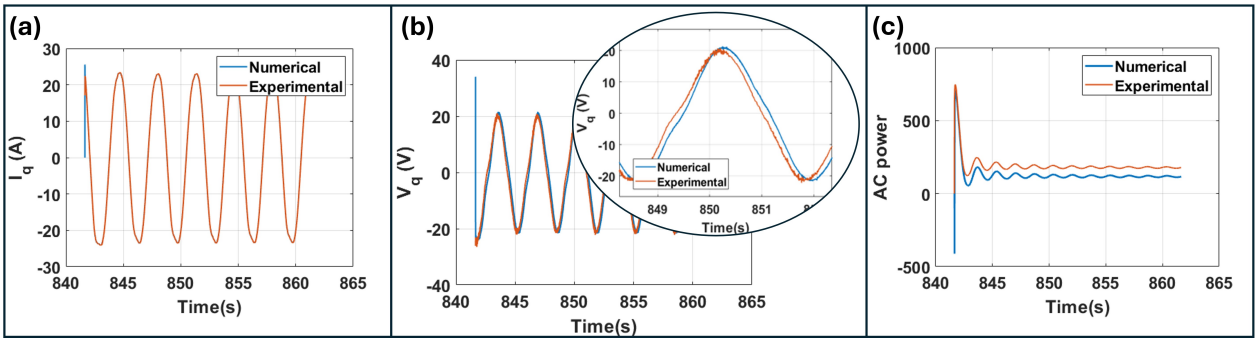

Figure 2: Comparison between the numerical prediction and experimental data in terms of Q-axis current, voltage, and AC power using manufacturer-provided parameters.

To fix this phase shift, the parameters of the motor are further tuned by using a trial-and-error method. It is found by lowering the stator resistance and the contribution of the last term in Eq. 2, the prediction of the Q axis voltage has a good agreement with the experimental data:

$$v_q = 0.6 R_s i_q + L_q \dot{i}_q + n_p \omega (i_d L_d + 0.9 \psi_m) \tag{18}$$

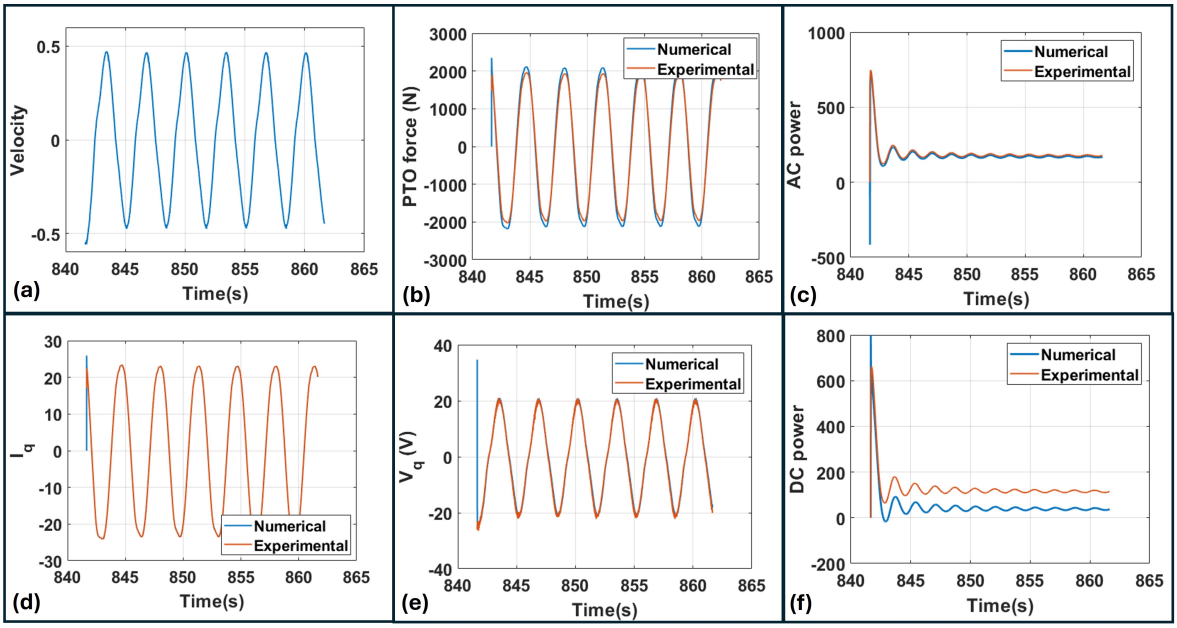

Figure 3: Complete PTO unit performance after tuning the motor parameters.

It is also worth noting that the 0.9 coefficient added to this equation represents a reduced contribution of the term rather than a reduced flux linkage (which would otherwise impact the motor torque calculation). The calibrated motor parameters are summarized in Table. 1.

The complete PTO unit performance after tuning the parameters is presented in Fig. 3. From this figure, we can see that the calibrated model now provides a good prediction of various system responses. Specifically, the phase shift of the Q axis voltage is now corrected (as shown in Fig. 3(e)), which leads to significantly improved accuracy in AC power prediction (Fig. 3(c): numerically simulated is 169.51W versus experimentally measured 178.43W, with only a 5% error). As presented in Fig. 3(b), the predicted PTO force is slightly larger than the experimental measurement, which may be due to mechanical losses and nonlinearities. Finally, although the improved model shows good agreement with the experimental data in terms of system responses, there still exists a significant mismatch in the DC power calculation, which requires tuning of the parameters in the inverter model.

Table 1: Calibrated Motor Parameters

Parameter (Motor)	Description	Value
L_d	d-axis inductance	52 mH
L_q	q-axis inductance	52 mH
R_s	Stator resistance	0.2898 Ohm
K_t	Torque constant	4.85 N/A
n_p	Number of pole pairs	24

3.2 Model Calibration: Inverter

The calibration of the inverter model focuses on matching the DC power generation, which is calculated by subtracting the inverter loss from the AC power. The inverter loss is mainly composed of conduction loss and switching loss, which are primarily affected by the resistance of the IGBT and diode, as well as the switch-on and switch-off losses. Therefore, the objective of the inverter model calibration is to identify the correct resistance and switch-on/off losses such that the model-predicted conduction and switching losses are in good agreement with the experimental data.

However, it is noted that the collected testing data does not naturally provide a breakdown of losses from AC to DC. Therefore, an assumption is made in this study to isolate different types of losses: the switching loss increases linearly with the increase of the switching frequency, while the conduction loss remains unaffected.

The experimental data is further processed according to this assumption. The corresponding wave condition has a height of 0.127m and a period of 3.3s. The experimental data covers the WaveBot performance under 4 different DC bus voltages: [125, 152, 226, 300.5]V, 5 different switching frequencies: [2000, 4000, 6000, 8000, 10000]Hz, and 9 different operational conditions (basically different PI gains for the hydrodynamic control) quantified by I_q: [14.2, 17, 18.3, 19.4, 20, 20.9, 22.55, 22.65, 24.35]A. To isolate the switching loss from the total losses, the loss data under a specific DC bus voltage (e.g., V_{dc} = 226V) and a specific operational condition (e.g., I_q = 20A), while with different switching frequencies, is selected. Based on the assumption, the change of the total loss subject to the switching frequency shall be only contributed by the switching loss. Therefore, the increment of the loss every 2000Hz of increase of the switching frequency is calculated (e.g., [6.7766, 6.8584, 6.6648, 7.2424]W), which is further averaged to compute the slope of the switching loss (which is impacted by the DC bus voltage and Q axis current):

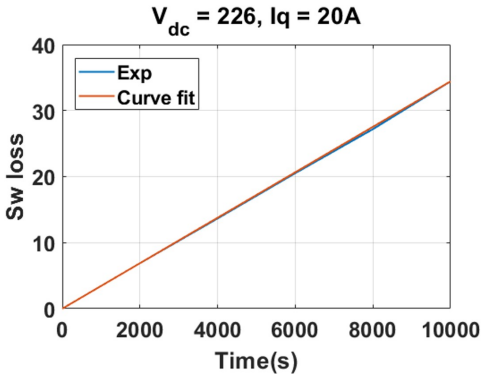

Figure 4: Linear curve fitting of the switching loss against the experimental data.

$$P_{sw} = c(V_{dc}, I_q)F_{sw} \tag{19}$$

The switching loss then can be computed at different switching frequencies (Fig. 4). After repeating this procedure for different DC bus voltage and Q axis current, the switching loss can now be isolated (as well as the conduction loss) from the total loss under varied operational conditions. Fig. 5 (a) and (c) show the breakdown of switching loss and conduction loss under different conditions from the experimental data. It is noted that the switching loss map is only presented for one DC bus voltage (226V).

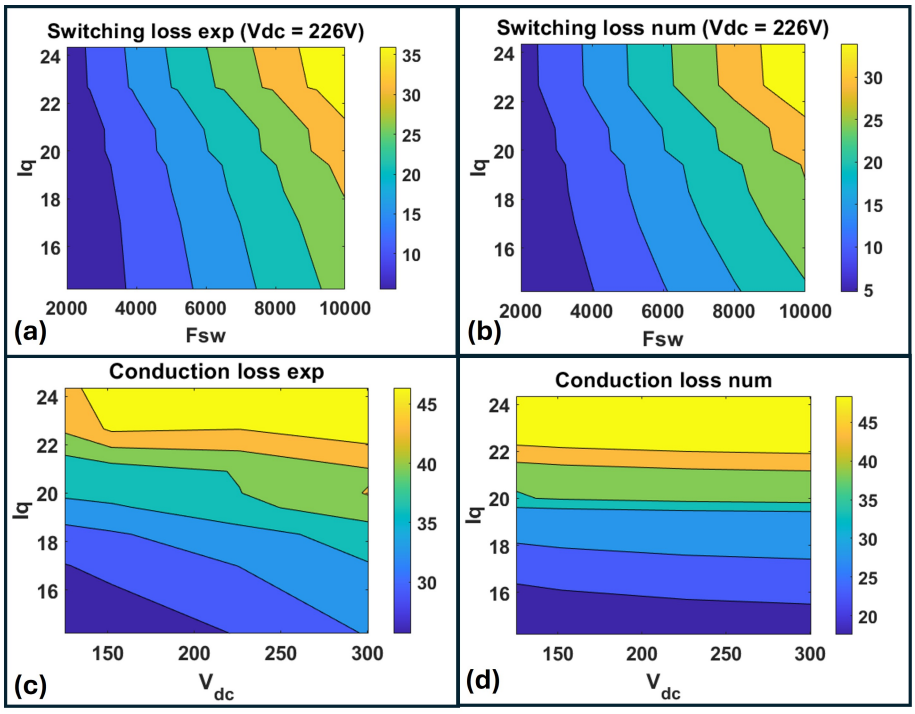

Figure 5: Comparison between the numerical prediction and experimental data in terms of switching loss and conduction loss.

According to the isolated switching loss and conduction loss from the experimental data, the resistance of the IGBT and diode are identified to be 0.231Ohm and 1.5×10^{-4}Ohm, respectively. Moreover, the switching on and off losses are identified to be 0.0577J and 0.0433J, respectively. The switching loss and conduction loss predicted by the calibrated inverter model are presented in Fig. 5 (b) and (d), which show good agreement between the numerical model and the experimental data. It is noted that the loss maps are generated according to 5s numerical simulations (instead of 20s, which is only applied for dedicated system response analysis, e.g., Fig. 6, which however shall be sufficient for electrical power to converge) due to the significant simulation cost (3.6hr for each case run for more than 100 cases). The Root Mean Squared Error (RMSE) for conduction loss prediction is around 5.8, and for switching loss is approximately 1.8. Finally, the calibrated inverter parameters are summarized in Table. 2.

Table 2: Calibrated Inverter Parameters

Parameter (IGBT)	**Description**	**Value**
R_{on}	On-state Resistance	0.231 Ohm
G_{off}	q-axis inductance	1×10^{-8} 1/Ohm
v_{th}	Threshold Voltage	0.6V
v_f	Forward Voltage	0.1V
$E_{on,0}$	Switch-on Loss	0.0577J
$E_{off,0}$	Switch-off Loss	0.0433J
Parameter (Diode)	**Description**	**Value**
$R_{on,d}$	On-state Resistance	1.5×10^{-4} Ohm
$G_{off,d}$	Off-state Resistance	1×10^{-8} 1/Ohm
$v_{f,d}$	Forward Voltage	0.1V
C_d	Junction Capacitance	50pF

3.3 Control performance

After the numerical model is calibrated based on the experimental data, the performance of the new control is assessed. The detailed system responses under the new control are presented in Fig. 6. The corresponding wave condition has a height of 0.127m and a period of 3.3s. It is noted that in addition to the minimized DC bus voltage, the switching frequency is also minimized to 2000Hz. As shown in Fig. 6(c), the DC bus voltage exhibits a clear time-varying pattern with a maximum value around 55.7835V and a minimum value around 10.1766V, which is significantly lower than the tested DC voltages (minimum 125V and maximum 300.5V). It is also evident that this small DC bus voltage is sufficient to supply the desired PTO force, as shown in Fig. 6(b) in terms of the Q axis current tracking.

Finally, with regard to power production, the generated mechanical, AC, and DC power are 321.7458W, 188.9081W, and 157.4694W, respectively. The resulting motor loss is 132.8377W, inverter conduction loss is 30.4191W, and switching loss is 1.0196W. Compared to an unoptimized PTO architecture (with DC voltage at 300.5V and switching frequency of 10kHz), where the inverter conduction loss is 40.5518W and switching loss is 42.1738W, the proposed control effectively reduces the inverter losses by 62%. The overall PTO efficiency is improved from 33% to 49%.

4 Conclusion

This paper presents the calibration of a high-fidelity PTO model using data obtained from a recent experimental campaign conducted by SNL at the MASK Basin for the WaveBot device. The high-fidelity model is composed of the motor and motor drive, which directly model the dynamic behavior of the switches and aim to provide an accurate prediction of different types of losses (e.g., motor conduction loss, inverter conduction loss, switching losses) in the drivetrain. By adjusting the model parameters, the numerical model shows good agreement with the experimental data in terms of system responses and power losses. In addition, a novel control that allows time-varying DC bus voltage is proposed in this research. The performance of the control is assessed using the calibrated model, and the simulation results show that the losses in the drivetrain can be effectively reduced by 62% with an optimal PTO architecture, significantly improving PTO efficiency by 48.5%. In the future, the research team plans to test this novel control on the WaveBot device to demonstrate its real-world performance.

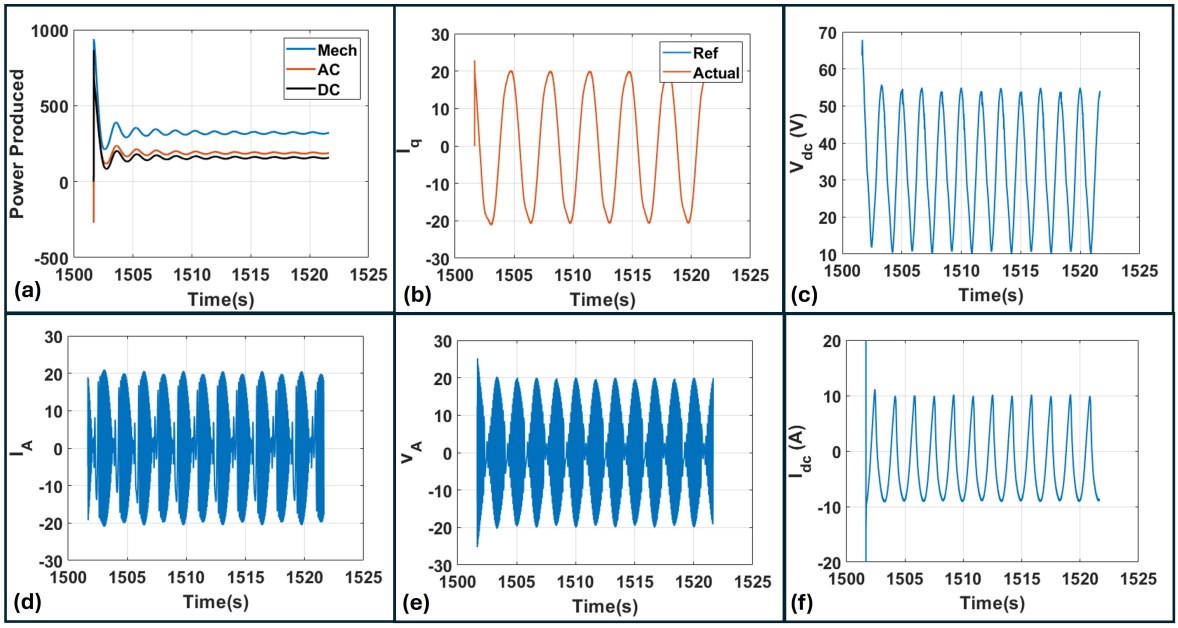

Figure 6: System responses of the PTO unit under the new control.

Acknowledgments

Sandia National Laboratories is a multimission laboratory managed and operated by National Technology & Engineering Solutions of Sandia, LLC, a wholly owned subsidiary of Honeywell International Inc., for the U.S. Department of Energy's National Nuclear Security Administration under contract DE-NA0003525.

References

[1] Benjamin Drew, Andrew R Plummer, and M Necip Sahinkaya. *A review of wave energy converter technology*. 2009.

[2] Johannes Falnes and Adi Kurniawan. *Ocean waves and oscillating systems: linear interactions including wave-energy extraction*. Vol. 8. Cambridge university press, 2020.

[3] Ryan G Coe, Giorgio Bacelli, and Dominic Forbush. "A practical approach to wave energy modeling and control". In: *Renewable and Sustainable Energy Reviews* 142 (2021), p. 110791.

[4] Giorgio Bacelli et al. "System identification of a heaving point absorber: Design of experiment and device modeling". In: *Energies* 10.4 (2017), p. 472.

[5] Madelyn G Veurink et al. "Wave energy converter direct drive power-take-off power electronic design to maximize power production". In: *2023 IEEE 24th Workshop on Control and Modeling for Power Electronics (COMPEL)*. IEEE. 2023, pp. 1–7.

[6] Tania Demonte Gonzalez et al. "Sliding mode control of a nonlinear wave energy converter model". In: *Journal of Marine Science and Engineering* 9.9 (2021), p. 951.

[7] Shangyan Zou et al. "Optimization of the electricity generation of a wave energy converter using deep reinforcement learning". In: *Ocean Engineering* 244 (2022), p. 110363.

[8] Bryson Robertson et al. "Holistic marine energy resource assessments: A wave and offshore wind perspective of metocean conditions". In: *Renewable Energy* 170 (2021), pp. 286–301.

[9] Shangyan Zou, Bryson Robertson, and Sanjaya Paudel. "Geospatial analysis of technical US wave net power potential". In: *Renewable Energy* 210 (2023), pp. 725–736.

[10] Shangyan Zou, Bryson Robertson, and Solomon Yim. "Practical power absorption assessment limits for generic wave energy converters". In: *Ocean Engineering* 277 (2023), p. 114303.

[11] Dongsheng Qiao et al. "Review of wave energy converter and design of mooring system". In: *Sustainability* 12.19 (2020), p. 8251.

[12] Ryan Geoffrey Coe et al. *Advanced WEC dynamics and controls MASK3 test*. Tech. rep. Sandia National Laboratories (SNL), Albuquerque, NM, and Livermore, CA ..., 2019.

[13] Hafiz Ahsan Said, Demián García-Violini, and John V Ringwood. "Wave-to-grid (W2G) control of a wave energy converter". In: *Energy Conversion and Management: X* 14 (2022), p. 100190.

[14] Marios Charilaos Sousounis et al. "Direct drive wave energy array with offshore energy storage supplying off-grid residential load". In: *IET Renewable Power Generation* 11.9 (2017), pp. 1081–1088.

[15] Shangyan Zou et al. "High-fidelity electric drivetrain modeling and control of a WaveBot wave energy converter". In: *The University Marine Energy Research Community (UMERC), Durham, USA, October 2023*.

[16] Dominic Forbush et al. *MASK4 Test Campaign for Sandia WaveBot Device*. Tech. rep. Marine and Hydrokinetic Data Repository (MHKDR); Sandia National ..., 2023.

[17] URL: https://www.alliedmotion.com/wp-content/uploads/documents/Megaflux_Frameless_Torque_Motors_MF0310_R7d.pdf.

[18] Ned Mohan, Tore M Undeland, and William P Robbins. *Power electronics: converters, applications, and design*. John wiley & sons, 2003.